Opto-Electronic Advances

CN 51-1781/TN ISSN 2096-4579 (Print) ISSN 2097-3993 (Online)

Double topological phase singularities in highly absorbing ultra-thin film structures for ultrasensitive humidity sensing

Xiaowen Li, Jie Sheng, Zhengji Wen, Fangyuan Li, Xiran Huang, Mingqing Zhang, Yi Zhang, Duo Cao, Xi Shi, Feng Liu and Jiaming Hao

Citation: Li XW, Sheng J, Wen ZJ, et al. Double topological phase singularities in highly absorbing ultra-thin film structures for ultrasensitive humidity sensing. *Opto-Electron Adv* **8**, 240091(2025).

https://doi.org/10.29026/oea.2025.240091

Received: 21 April 2024; Accepted: 28 August 2024; Published online: 28 March 2025

Opto-Electronic Advances

Article

March 2025, Vol. 8, No. 3

DOI: 10.29026/oea.2025.240091 CSTR: 32247.14.oea.2025.240091

Double topological phase singularities in highly absorbing ultra-thin film structures for ultrasensitive humidity sensing

Xiaowen Li[1,2†], Jie Sheng[2†], Zhengji Wen[3], Fangyuan Li[2], Xiran Huang[2], Mingqing Zhang[1], Yi Zhang[2], Duo Cao[2], Xi Shi[2*], Feng Liu[2*] and Jiaming Hao[1*]

Phase singularities (PSs) in topological darkness-based sensors have received significant attention in optical sensing due to their rapid, ultra-sensitive, and label-free detection capabilities. Here, we present both experimental and theoretical investigations of an ultrasensitive and multiplexed phase-sensitive sensor utilizing dual topological PSs in the visible and near-infrared regions. This sensor uses a simple structure, which consists of an ultra-thin highly absorbing film deposited on a metal substrate. We demonstrate the achievement of dual-polarization darkness points for s- and p-polarizations at different incident angles. Furthermore, we theoretically explain the double topological PSs accompanied by a perfect ±π-jump near a zero-reflection point, based on the temporal coupled-mode formalism. To validate its multifunctional capabilities, humidity sensing tests were carried out. The results demonstrate that the sensor has a detection limit reaching the level of 0.12 ‰. These findings go beyond the scope of conventional interference optical coatings and highlight the potential applications of this technology in gas sensing and biosensing domains.

Keywords: double topological darkness; phase singularity; thin-film optics; ultrasensitive sensing

Li XW, Sheng J, Wen ZJ et al. Double topological phase singularities in highly absorbing ultra-thin film structures for ultrasensitive humidity sensing. *Opto-Electron Adv* **8**, 240091 (2025).

Introduction

The concept of phase singularities (PSs) is defined to describe a phenomenon that exhibits zero reflection/transmission (also referred to as the darkness point) of light accompanied by a rigorous Heaviside π-phase jump in an optical system[1–6]. The effect of ultrafast changes of phase and amplitude close to the PS (zero-reflection point), enables strong manipulation of light and promises several important applications, particularly, in the field of optical sensing[2–8]. Unlike the field of optical sensing achieved through Bound States in the Continuum (BIC), which is extensively studied and depends on high Q-factors and low mode volumes for absorption, reflection, or transmission[9–11]. However phase singularities instead focus on their phase changes[12–14]. Furthermore, conventional optical PS systems, such as metamaterials[15–21], have

[1]Institute of Optoelectronics & Department of Materials Science, Shanghai Frontiers Science Research Base of Intelligent Optoelectronics and Perception, Fudan University, Shanghai 200433, China; [2]Department of Physics, Shanghai Normal University, Shanghai 200234, China; [3]State Key Laboratory of Infrared Physics, Shanghai Institute of Technical Physics, Chinese Academy of Sciences, Shanghai 200083, China.

[†]These authors contributed equally to this work.

*Correspondence: X Shi, E-mail: xishi@shnu.edu.cn; F Liu, E-mail: fliu@shnu.edu.cn; JM Hao, E-mail: jmhao@fudan.edu.cn

Received: 21 April 2024; Accepted: 28 August 2024; Published online: 28 March 2025

an extremely tight tolerance for fabrication errors or inherent roughness of thin films and patterns. In recent years, there has been extensive research attention on topological PS due to their topologically protected features[1,18–24]. The topological PS is resistant to small deformations or defects in the physical system, reducing the difficulties in device fabrications and guaranteeing its reproducibility and reliability. General methods for achieving topological PS are typically demonstrated using plasmonic nanostructures[16,19], and Fabry-Pérot microcavities[22,24,25]. The underlying physics of the optical phase control is achieved through modulating wave vectors in momentum space or gradual accumulation within nearly transparent dielectric layers. Traditionally, modulating wave vectors requires complex nanostructures, while Fabry-Pérot microcavities require optical wavelength-scale thickness. Topological PSs in atomically thin high-refractive-index materials (2D materials)[1,26] have also been recently observed, but these systems support only single polarization (p- or s- polarization) for topological darkness.

In contrast to single topological PS systems capable of detecting only one target at a time, double topological PSs have the potential to simultaneously differentiate multiple targets. This capability arises from their ability to be designed to match the vibrational modes of distinct sensing targets[17,19]. Moreover, the utilization of double (p- and s-) topological PS sensing relies on phase changes rather than light intensity. Thus, it can avoid challenges such as interference disturbance and external filtering commonly encountered in traditional multiple target detection systems[27–33]. Nevertheless, achieving PSs in double topological darkness, particularly for s-polarization, presents a formidable challenge. Achieving s-polarized darkness requires materials exhibiting magnetic responses, which are seldom found in natural materials. To achieve s-polarization darkness, researchers have employed two approaches to solve the aforementioned challenge using artificial optical materials. One approach involves the utilization of complex optical engineering structures, such as surface relief gratings[24], cross-potent metaparticles[34,35], or split-ring resonators[36,37]. Manipulation of the complex refractive index ($n_{\mathrm{eff}}(\lambda)$, $k_{\mathrm{eff}}(\lambda)$) plane[18,25] of these structures is undertaken to obtain the desired magnetic response. This necessitates the application of sophisticated lithography techniques for nanostructure fabrication, with stringent requirements for machining accuracy and defect minimization. In response to these challenges, an alternative approach for achieving s-polarization darkness involves the utilization of lithography-free planar multilayer film stacks, such as one-dimensional photonic crystals (PCs)[17], and optical cavities[2,3,38] operating at visible and infrared frequencies. The large wavelength-scale and multilayer interface characteristics of these structures may lead to optical phase accumulation. The PS of s-polarization topological darkness can be realized through interface interference. Both PSs of s-polarization and p-polarization can be achieved by growing a lossless dielectric film on an absorbing substrate[2,22], or by utilizing asymmetric Fabry-Pérot microcavities[3]. Although implementing these lithography-free nanostructures is relatively easy in production, the medium's thickness must be on the order of the optical wavelength.

In this study, we present a novel, cost-effective, lithography-free, ultrasensitive, and multiplexed phase-sensitive sensor architecture. The sensor comprises an ultrathin ($h << \lambda/4n$) highly absorbing dielectric layer of germanium (Ge) layer deposited on a silver (Ag) film. The experiment demonstrates the emergence of topological PS for both p- and s-polarization darkness across visible and near-infrared frequencies. By calculating the zero reflection surface (ZRS) for p- and s-polarization, we identified intersections with the dispersion curve of Ge ($n(\lambda)$, $k(\lambda)$, λ) at two points, thus stimulating the PSs effect associated with double topological darkness. The phase jump of double topological darkness is calculated using the transfer matrix method. Furthermore, we analyzed the topological PS of polarization darkness based on temporal coupled-mode theory. Our studies reveal abrupt ±π-jumps in the phase parameter near zero-reflection, plotted as a function of wavelength for a fixed incidence angle proximal to the PS. The experimental results are rigorously validated through theoretical simulations. To demonstrate the functionality of our proposed phase-sensitive sensing device, we applied it to a humidity sensing system by spin-coating a thin layer of humidity-sensitive material, polyvinyl alcohol (PVA), onto the device. Experimental results show that the sensor exhibits a detection limit of 0.13 ‰ for p-polarization, and 0.12‰ for s-polarization. Furthermore, by introducing a figure of merit (FOM) defined as the ratio of the phase change ($\mathrm{d}\Delta$) to the amplitude change ($\mathrm{d}\Psi$) under varying of humidity conditions, FOM = $\mathrm{d}\Delta/\mathrm{d}\Psi$ we achieved FOM values of 2450 and 425 for p- and s-polarized waves. The results significantly outperform those reported in prior studies[3,21].

Results

Double topological PSs for s- and p-polarizations in ultra-thin highly absorbing film structures

We present an ultrasensitive and multiplexed phase-sensitive sensor utilizing double topological PSs. The sensor architecture comprises a deposited ultra-thin ($h << \lambda/4n$) absorbing dielectric Ge layer on an Ag film. As a semiconductor, Ge has a bandgap below the photon energies within the visible and infrared spectral ranges, resulting in rapid light attenuation. When combined with metals possessing finite optical conductivity, this structure enables effective phase accumulation. This phenomenon arises from interface reflection and transmission phase shifts occurring within a sub-wavelength optical path. While extensively utilized in structural colors applications[39,40], this novel physical mechanism is rarely reported in the context of topological PS. To demonstrate how an ultrathin highly absorbing medium film on a metal substrate exhibits double polarization topological darkness, consider the scenario of light reflection from a planar structure, as shown in Fig. 1(a). An ultra-thin absorbing dielectric layer with a thickness of t = 26 nm is placed on top of a metal substrate. For a given thickness of the dielectric film, angle of incidence (θ), wavelength (λ), and polarization (s- or p-wave), reflection from the structure can be made exactly zero. This imposes two conditions on the parameters (as we require that both real and imaginary parts of complex reflection coefficient $r(n, k, \theta, \lambda)$ should be zero simultaneously) and implies that for each given combination of n and k of the effective medium layer (EML) we can find both wavelength $\lambda(n, k)$ and incidence angle $\theta(n, k)$ that provide exactly zero reflection for the structure[22,25]. Plotted in (n, k, λ) coordinates, this procedure yields a continuous surface which we refer to as a zero reflection surface (ZRS), Fig. 1(b). (p-polarization ZRS_p marked by the solid blue ball, and s-polarization ZRS_s in red). The dispersion curve of the Ge layer, represented by the yellow line, is plotted on the same 3D graph. Two points of intersection, marked by yellow dots, exist between the dispersion curve of the Ge layer and the ZRS. Meanwhile, to demonstrate that the proposed structure is topologically protected, we simulate the defects of Ge material in experiments by varying the refractive index (n, k) of Ge by ±10% in Fig. S2.

Experimentally, we deposited a 26 nm thickness layer of Ge onto an Ag substrate. The cross-sectional and surface scanning electron microscopy (SEM) images of the sample are presented in Fig. S3. Figure 2(a) and 2(b) illustrate p-polarized darkness and s-polarized darkness across various wavelengths and angles of incidence. Additionally, Fig. 2(c) and 2(d) display the false-color 2D reflectance spectra for p- and s-polarization, obtained through the transfer matrix method (TMM). Experimental measurements span an angle range from 6° to 85°, while TMM calculations cover 0° to 85°. Reflectance spectra, measured from 400 nm to 1600 nm at different angles of incidence, are presented in Fig. 2(e) and 2(f). Remarkably, excellent agreement is observed between experimental data and calculations. Specifically, p-polarization exhibits zero reflection at an incidence angle of 80.2° and wavelength of 587.8 nm, while s-polarization achieves zero reflection at 29.4° and wavelength of 937.1 nm. Yellow circles represent regions where polarization

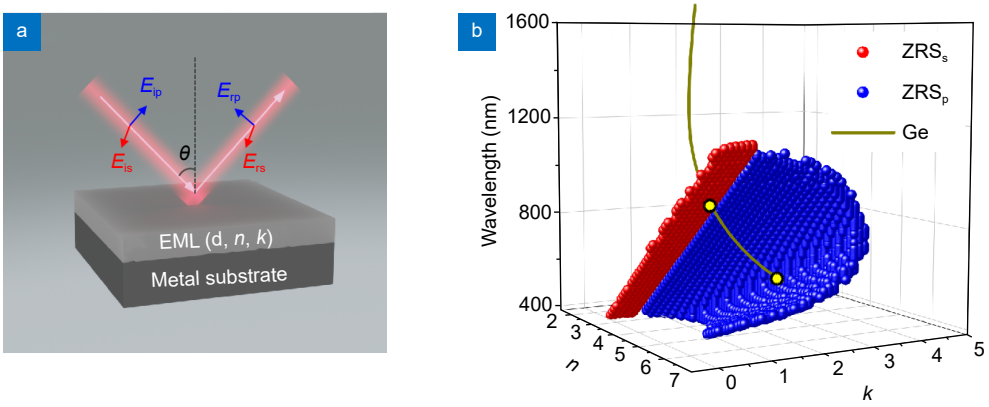

Fig. 1 | Theoretical predictions of double topological darkness (zero-reflections). (**a**) Schematics of light reflection for observing PSs from the ultra-thin absorbing dielectric on a metal substrate. The effective medium layer (EML) has fixed thickness. (**b**) The yellow point of intersection of spectral dispersion curve $n(\lambda)$, $k(\lambda)$ of the top layer Ge with the ZRS with a blue point for p-polarized light and ZRS with a red point for s-polarized light are topologically protected.

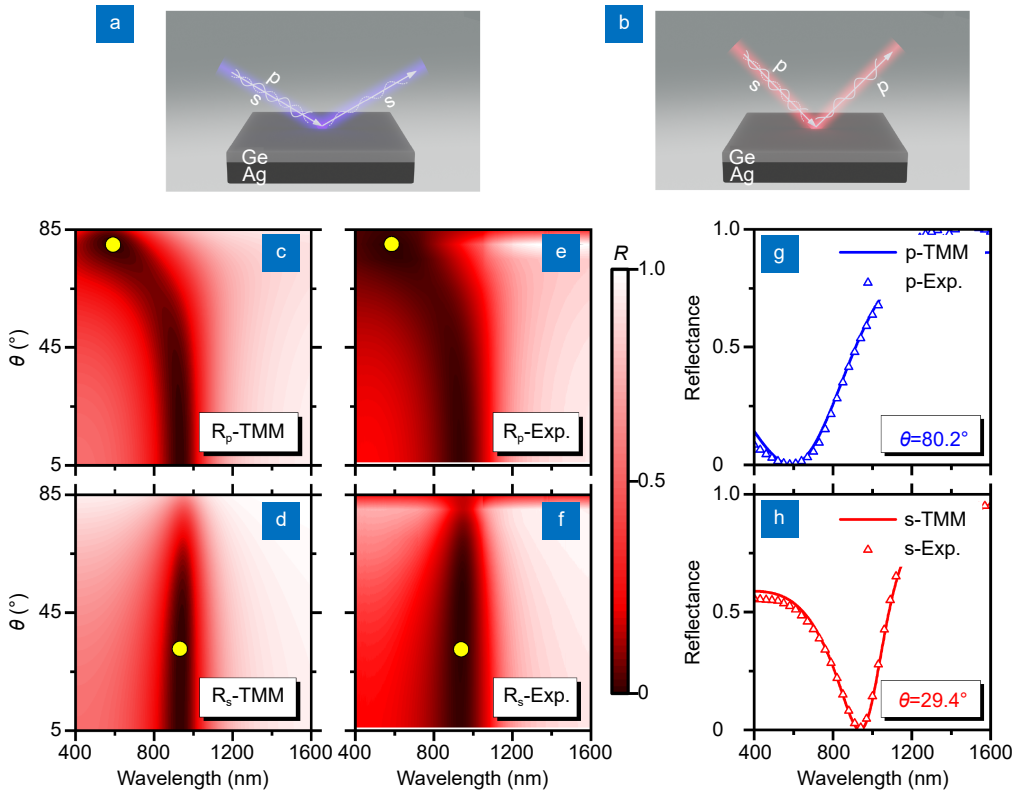

Fig. 2 | Double topological PS effect in ultra-thin absorbing dielectric structures. Schematic of the Ge (26 nm)/Ag system exhibiting: (**a**) p-polarized topological darkness point effect, and (**b**) s-polarized topological darkness point effect. TMM calculated angular reflectivity spectra for: (**c**) p-polarized and (**d**) s-polarized reflectance spectrum of the thin-film absorber. (**e**, **f**) show the reflectance measurements, respectively. The yellow circle regions refer to wavelength and angle pairs where the polarization darkness points occur for p-polarized light and s-polarized light. Reflectance spectra are shown for p-polarization at (**g**) 80.2° and for s-polarization at 29.4°, with measured data represented by hollow triangles and calculated data by solid lines.

darkness points occur for p- and s-polarized light. Furthermore, to illustrate zero reflection, reflectance spectra for p- and s-polarized light at the two angles (80.2° and 29.4°) are presented in Fig. 2(g) and 2(h), with experimental measurements represented by hollow triangles and calculations shown by solid lines. Evidently, the thin-film absorber supports two modes within the wavelength range of interest for both p- and s-polarizations.

To further clarify the PS, we characterize our samples using spectroscopic ellipsometry, as schematically depicted in Fig. 2. Details can be found in the Methods section 4.2. Ellipsometry measures the ratio of the p- and s-polarized reflection coefficients, ρ, expressed as Ψ and Δ[41]:

$$\rho = \frac{r_{\rm p}}{r_{\rm s}} = \tan\Psi e^{i\Delta}\,, \tag{1}$$

here, $r_{\rm p}$ and $r_{\rm s}$ are respectively the p- and s-polarized Fresnel amplitude reflection coefficients. The amplitude of ρ ($\tan\Psi$) is the ratio of the moduli of $r_{\rm p}$ and $r_{\rm s}$, while the phase of ρ (Δ) gives the difference between the phase shifts experienced by p- and s-polarized light on reflection. Therefore, ellipsometry provides us with information not only about the reflected light amplitude but also about the light phase.

The false-color 2D plots illustrating the phase spectra of ellipsometry parameters Ψ and Δ, derived from the TMM, are shown in Fig. 3(a) and 3(c), respectively. Concurrently, phase spectra measurements obtained using a spectroscopic ellipsometer are presented in Fig. 3(b) and 3(d). Remarkably, the measured amplitude parameter in Fig. 3(b) and Δ in Fig. 3(d) exhibit excellent agreement with the simulated spectrum in Fig. 3(a, c), calculated using the TMM. Our spectroscopic ellipsometer source emits wavelengths ranging from 400 nm to 1600 nm, with test angle of incidence ranging from 45° to 85°. The spectra of Ψ unequivocally demonstrate the attainment of exact zero in p-polarized light at the dip where Ψ reaches the incident angle of 80.2° and wavelength of 587.8 nm, while Ψ equals 90° with a peak at 29.4° and wavelength of 937.1 nm in s-polarized light. Correspond-

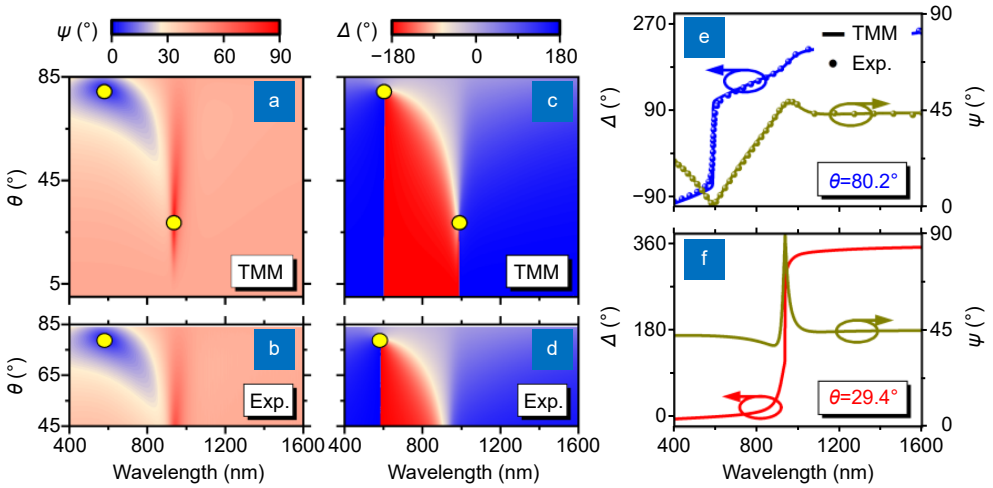

Fig. 3 | Experimental observation of PSs. (**a–c**) Simulated and (**b–d**) experimental ellipsometric parameters amplitude (Ψ) and phase (Δ) for Ge (26 nm)/Ag system. The yellow circle regions refer to wavelength and angle pairs where the topological PSs for p-polarized light (Ψ = 0° at 80.2° 587.8 nm) and s-polarized light (Ψ = 90° at 29.4° 937.1 nm) occur. (**e**, **f**) Ellipsometry parameters Ψ and Δ at the above two angles (80.2° and 29.4°) for p- and s-polarized light, represented by solid circles for measured data and solid lines for TMM calculations.

ingly, the ellipsometric phases Δ in Fig. 3(c) and 3(d) clearly demonstrate that the reflected phase at these points, known as PS, is undefined. To show the PS, ellipsometry parameters Ψ and Δ at two angles (80.2° and 29.4°) for p- and s-polarized light are depicted in Fig. 3(e) and 3(f), where measured data is represented with solid circles, while calculated is presented with solid lines. Δ shows a significant jump with Ψ equaling 0° or 90°. Overall, our experimental findings prove that double polarization darkness points are indeed PSs, occurring if and only if the response function (reflection in our case) exhibits zero magnitude at that point.

PSs and topological darkness in thin-film absorbers: a temporal coupled-mode theory

The temporal coupled-mode theory (TCMT) offers analytical insights into resonance systems, including waveguides, optical resonators, photonic crystals, metamaterials, and other structures[15,42–44]. In this study, we employ TCMT to describe topological darkness and PSs.

To establish a comprehensive framework, we commence with a multiport system illustrated in Fig. 4(a). This system exhibits mirror symmetry and supports m resonant modes. To derive explicit expressions, we introduce the main equations of TCMT and the scattering matrix, considering the symmetry of the thin-film slab:

$$\frac{\mathrm{d}A}{\mathrm{d}t} = (-\mathrm{i}\omega_0 - \gamma - \gamma_0)A + \boldsymbol{K}^{\mathrm{T}}\boldsymbol{s}^{+} , \tag{2}$$

$$\boldsymbol{s}^{-} = \boldsymbol{S}\boldsymbol{s}^{+} = \boldsymbol{C}\boldsymbol{s}^{+} + \boldsymbol{D}A , \tag{3}$$

here, A represents the resonance amplitude, ω_0 is the mode's resonant frequency, γ_0 is the decay rate of intrinsic loss, and γ is the decay rate due to radiation. The vectors $\boldsymbol{s}^{+}=(\ \boldsymbol{E}_1^{+}\ \cdots\ \boldsymbol{E}_i^{+}\ \cdots\ \boldsymbol{E}_n^{+}\ )$ and $\boldsymbol{s}^{-}=(\ \boldsymbol{E}_1^{-}\ \cdots\ \boldsymbol{E}_i^{-}\ \cdots\ \boldsymbol{E}_n^{-}\ )$ represent incoming and outgoing waves, respectively, and $\boldsymbol{S}$ is the scattering matrix. $\boldsymbol{K}$ and $\boldsymbol{D}$ denote the coupling coefficients between the resonance and the ingoing and outgoing plane waves.

The theoretical model involves optical resonators coupled with 'm' ports, where 'm' is labeled as '1s, 1p, 2s, 2p' (refer to Fig. 4(b)). Additional derivation details can be found in the Supplemental information Section 1. Subsequently, we can derive the ellipsometric parameters:

$$\Psi = \tan^{-1}\left|\frac{r_{\mathrm{pp}}}{r_{\mathrm{ss}}}\right| , \tag{4}$$

$$\Delta = \varphi_{\mathrm{p}} - \varphi_{\mathrm{s}} = \mathrm{angle}\left(1 + \frac{2\gamma_p}{\mathrm{i}(\omega - \omega_{\mathrm{p0}}) - \gamma_{\mathrm{p}} - \gamma_{\mathrm{p0}}}\right) - \mathrm{angle}\left(1 + \frac{2\gamma_{\mathrm{s}}}{\mathrm{i}(\omega - \omega_{\mathrm{s0}}) - \gamma_{\mathrm{s}} - \gamma_{\mathrm{s0}}}\right) . \tag{5}$$

Values extracted from fitting curves (solid lines in Fig. 4(c) and 4(d)) are shown in Table 1. All parameters including ω_{s0}, γ_{s}, γ_{s0}, and γ_{p0}, γ_{p}, γ_{p0} are fitted. From Fig. 4(c) and 4(d), it is observed that the theoretical model results are in good agreement with the experimental results in the vicinity of topological points. The phase difference Δ exhibits a jump of 168.7° for the p-polarization

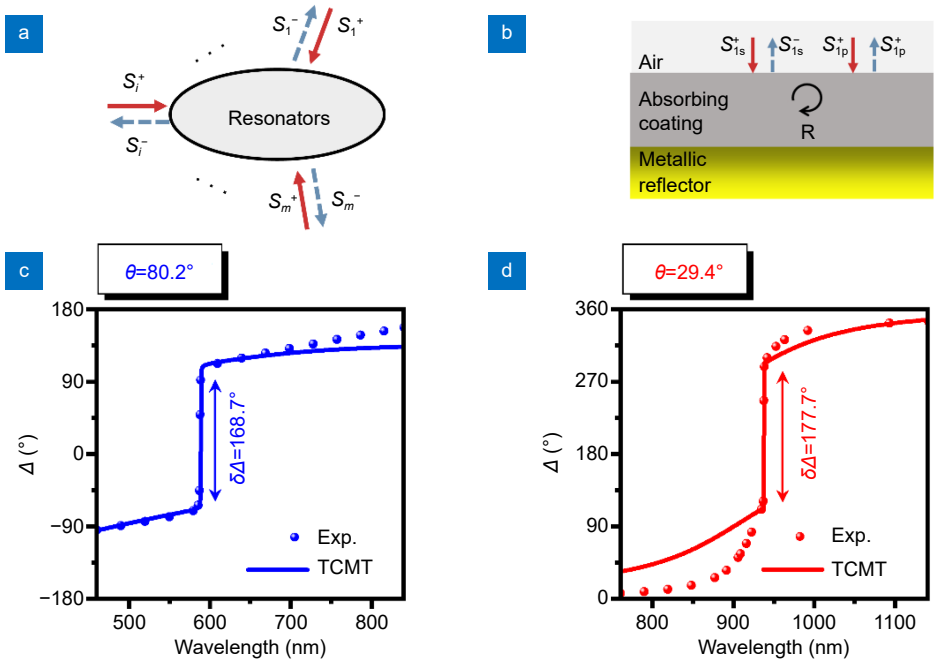

Fig. 4 | Topological nature of darkness points associated with spectral PSs. (**a**) Schematic of the multi-port multimode system. (**b**) Analyses using a multiple scattering model along with the thin-film system to determine the typical reflection phase. (**c**, **d**) Investigation of the ellipsometry parameters Ψ and Δ at the aforementioned angles (80.2° and 29.4°) for p- and s-polarized light, measured with solid circles and calculated using TCMT represented by solid line.

Table 1 | Values extracted for double topological darkness points.

Type[a)]	ω_{s0}	γ_s	γ_{s0}	ω_{p0}	γ_p	γ_{p0}
29.4°	2010	185.6	185.6	2040	264.9	210.0
80.2°	1985	38.5	194.0	3200	840.0	839.2

[a)](The unit of ω and γ is 10^{12}*rad/s.)

topological darkness point and 177.7° for the s-polarizations. We infer that the discrepancy between the theoretical and experimental results in the wavelength region far from the topological points mainly originates from the contribution of high order resonances outside the frequency range our investigation.

Humidity sensing with polyvinyl alcohol on thin-film optical PS sensor

From an application standpoint, we illustrate the potential of our PS sample to function as a sensor for label-free multichannel applications. Leveraging the PS behavior of our devices at the dark points, we can detect changes in the optical properties of the thin-film device for humidity sensing. To demonstrate this, we apply a spin-coated PVA layer on the highly absorbing media-metal substrate light absorber to detect humidity concentrations. Fig. 5(a) and 5(b) depict a p-polarized point of darkness and an s-polarized point of darkness, respectively. Research shows that p-polarization exhibits zero reflection at an incidence angle of 73.0° and wavelength of 738.0 nm, and 48.0°/ 939.3 nm for s-polarization. To illustrate the PS of the new structure, ellipsometry parameters Ψ and Δ at the two angles (73.0° and 48.0°) for p- and s-polarized light are investigated in Fig. 5(c) and 5(d), with solid circles representing measured values and solid lines indicating calculated values. Likewise, Δ exhibits a significant π-jump with $\Psi = 0°$ or $\Psi = 90°$.

Notably, the volume of PVA, a typical hydrogel, exhibits sensitivity to environmental humidity, swelling upon absorption of water molecules from the surrounding air[45,46]. The dielectric permittivity of PVA was measured via ellipsometry (Fig. S4). Subsequently, utilizing PVA as the sensor core layer enables the dynamic adjustment of the thin-film thickness upon exposure to humid air, resulting in distinct jumps in the values of Δ in real-time. Exploiting this dynamic behavior facilitates high-sensitivity humidity sensing.

The ellipsometry parameters Ψ and Δ of the PVA/Ge/Ag system measured at an angle of 73.0° are

shown in Fig. 6(a) and 6(b), respectively. The reflection spectra are shown in Fig. S5(a). As anticipated, the jump in Δ exhibited significant variation with increased humidity. The magnified view highlights the capacity to modulate Δ at 73.0° by adjusting the humidity of air. Additionally, in Fig. 6(b), the magnified view reveals deviations of Ψ from 0 with changing air humidity. This deviation can be attributed to the destruction of perfect absorption due to the increased thickness of the PVA thin-film under higher humidity conditions.

In Fig. 6(c), we illustrate the jump of Δ associated with increased humidity from 734.3 nm to 741.6 nm. To quantitatively analyze the relative sensitivity S of the jump with Δ, we define $S_{\delta\Delta} = (\delta\Delta_1 - \delta\Delta_2) / (H_1 - H_2)$, where $\delta\Delta_1$ and $\delta\Delta_2$ represent the jumps with Δ for different air humidities (H_1 and H_2) at the PS point, respectively. The relative sensitivity was found to be 7.52°(1%)$^{-1}$ when the humidity ranged from 40% to 50% and 4.1°(1%)$^{-1}$ when the humidity ranged from 40% to 80%. For ellipsometry parameters Ψ, $S_{\lambda\Psi\min} = (\lambda_{\Psi\min1} - \lambda_{\Psi\min2}) / (H_1 - H_2)$, where $\lambda_{\Psi\min1}$ and $\lambda_{\Psi\min2}$ represent the minimum values of Ψ for different air humidities at the PS point, representing the resonance peak wavelength. The sensitivity was calculated to be 0.29 nm(1%)$^{-1}$ when the humidity ranged from 40% to 80%, which is relatively smaller owing to the resonance of the structure topologically protected. This suggests that the phase-sensitive measurement at the PS point can achieve an order of magnitude improvement in relative sensitivity compared to that of the conventional resonance peak wavelength. The accuracy of phase jump measurements in the experimental setup was 0.1°, we can thus estimate the detection limit of humidity sensing for the proposed structure (p- polarization) to be at the level of ~0.13‰.

Similarly, the measured ellipsometry parameters Ψ and Δ of s-polarization darkness points with the PS at 48.0° are shown in Fig. 7(a) and 7(b). The reflection spectra are shown in Fig. S5(b). These plots illustrate the spectra of Ψ and Δ under different air humidities of the PVA/Ge/Ag system. The phase jump $\delta\Delta$ and the variations in resonance peak wavelength $\delta\lambda_{\Psi\min}$ with increasing humidity are shown in Fig. 7(c) and 7(d). Experimentally, the sensitivity values were $S_{\delta\Delta}$ = 8.41°(1%)$^{-1}$ and $S_{\lambda\Psi\min}$= 0.07 nm(1%)$^{-1}$ with humidity ranging from 40% to 50%, and $S_{\delta\Delta}$ = 3.83°(1%)$^{-1}$ and $S_{\lambda\Psi\min}$= 0.07 nm(1%)$^{-1}$ with humidity ranging from 40% to 80%. The detection limit of humidity sensing for the structure operating in s-polarization state can be as high as 0.12‰. Furthermore, by introducing a figure of merit (FOM) defined as the ratio of the phase change (dΔ) to the amplitude change (dΨ) under varying of humidity conditions, FOM = dΔ/dΨ, we achieved FOM values of 2450 and 425 for p- and s-polarized waves. The results significantly outperform those reported in prior studies[3,21]. Finally, to

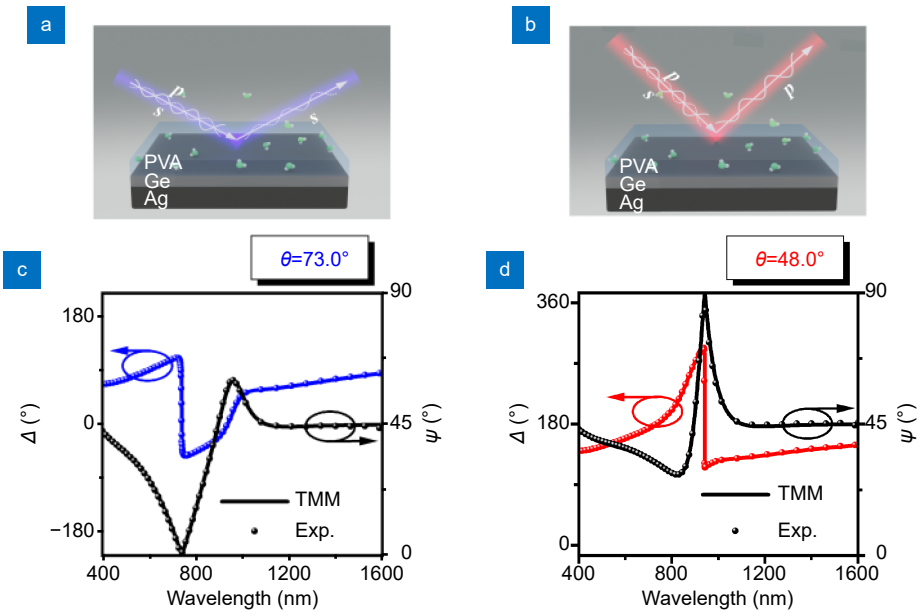

Fig. 5 | Double topological PSs in ultrathin absorbing dielectric structures with PVA film. Schematic of the PVA (40 nm)/Ge (26 nm)/Ag system exhibiting (**a**) the p-polarized topological darkness point effect and (**b**) the s-polarized topological darkness point effect. (**c**, **d**) Investigation of the ellipsometry parameters Ψ and Δ at the aforementioned angles (73.0° and 48.0°) for p- and s-polarized light, measured with solid circles and calculated using TMM represented by solid lines.

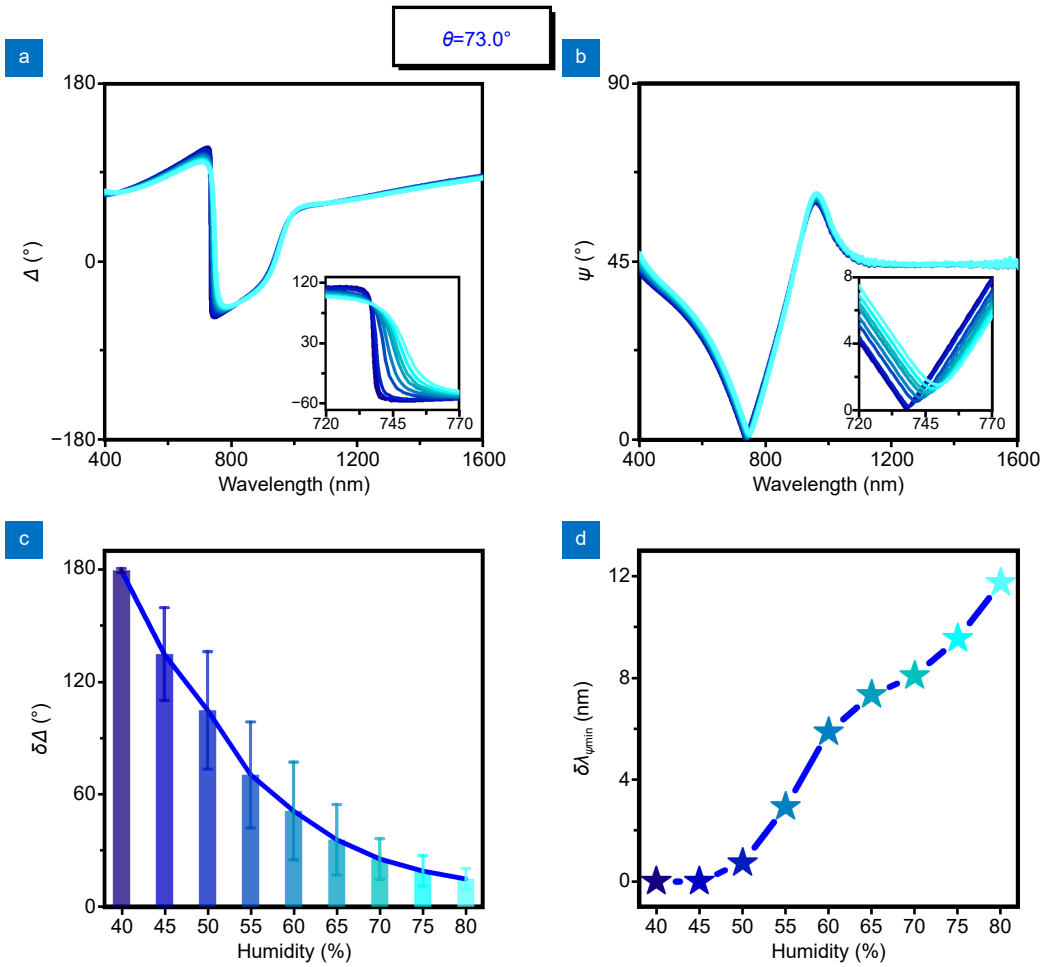

Fig. 6 | Humidity sensor based on topology of PVA film on Ge/Ag. (**a**, **b**) The dependence of ellipsometric parameters Δ and Ψ on the humidity of air recorded at the incidence angle of 73.0° with p-polarization topological darkness points, corresponding to the PS. The insets show the magnified view of Δ and Ψ. (**c**) The jump of Δ with increased humidity at λ = 734.3 nm to 741.6 nm. The error bars represent the standard deviation of multiple measurements. (**d**) Spectral shift of the resonance position of Ψ spectrum with increased humidity of air.

verify the reliability of the experimental humidity sensing results, a series of tests were conducted, which confirmed the good repeatability of the measurements (see Fig. S8 in Supplementary information). These findings collectively indicate that our proposed topological PS of double polarization darkness points indeed exhibits ultrasensitive sensing and holds significant potential as a multi-site optical gas sensor.

Conclusion

In summary, we have developed a formal framework for the double topological PS in ultra-thin ($h << \lambda/4n$) absorbing dielectric film structures. The structure architecture comprises a deposited 26 nm Ge layer on an Ag film. Experimental demonstrations have confirmed the presence of a topological darkness point accommodating both s- and p-polarized light, where the light reflection ceases entirely. Notably, we have established a comprehensive theoretical model describing transport processes across multiple input and output ports, including both s- and p-polarization channels, through a multimode optical resonator embedded in a thin-film set up. Theoretical analyses have revealed that the phase behavior of the ellipsometry parameter Δ exhibits abrupt π-jumps proximate to a zero-reflection point. Capitalizing on the high phase sensitivity near the topological darkness point, the discernment of minute variations in the electromagentic milieu of the thin-film device is facilitated, enabling the development of a lithography-free, ultrasensitive platform. Notably, we demonstrated the feasibility of a humidity sensor using readily available and cost-effective materials, without the necessity for nanofabrication. The device also holds potential as a platform for other sensors, particularly, for the development of

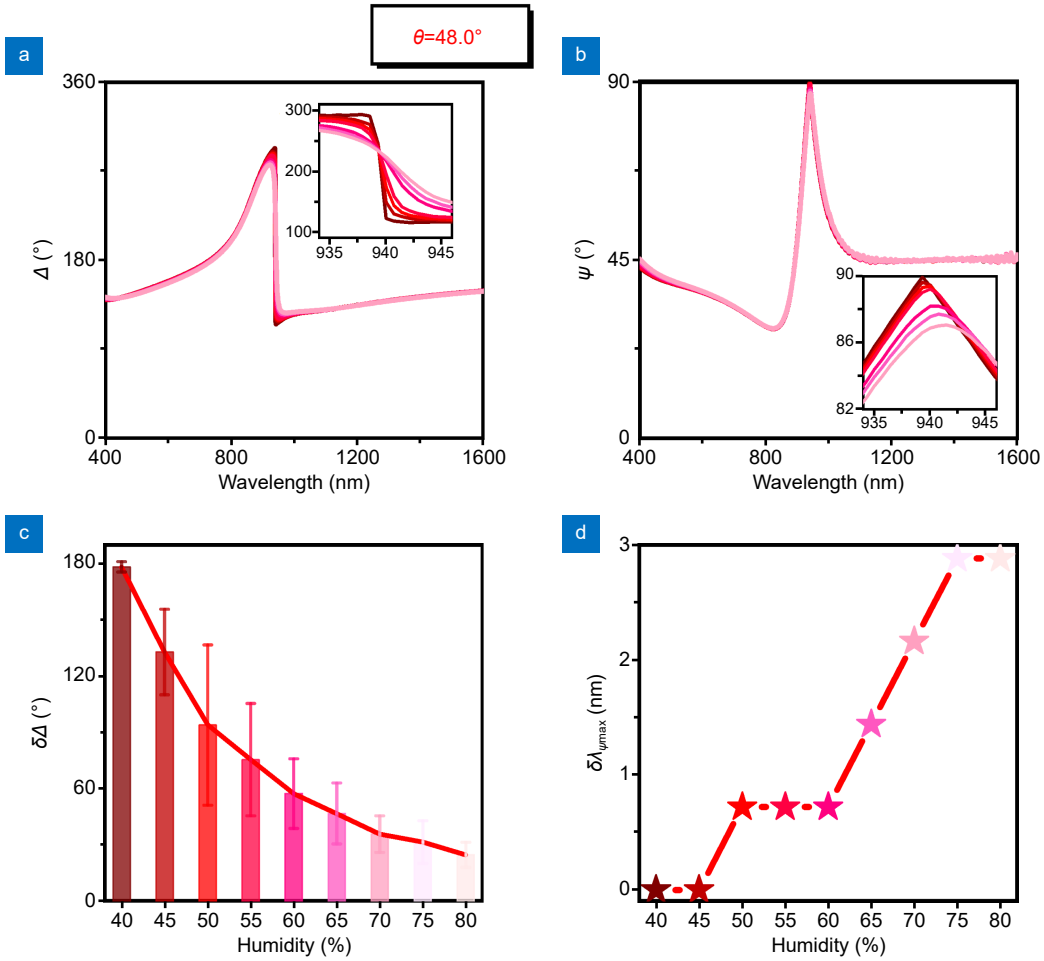

Fig. 7 | Humidity sensor based on topology of PVA film on Ge/Ag. (a, b) The dependence of ellipsometric parameters Δ and Ψ on the humidity of air recorded at the incidence angle of 48.0° with s-polarization topological darkness points, corresponding to the PS. The insets show the magnified view of Δ and Ψ. (c) The jump of Δ with increased humidity at λ = 937.8 nm to 940.7 nm. The error bars represent the standard deviation of multiple measurements. (d) Spectral shift of the resonance position of Ψ spectrum with increased humidity of air.

cost-effective apta-biosensor platforms. The double topological PS effect can be used to realize polarizers for both s- and p-polarizations, as well as ultrafast polarization switches. Furthermore, it can find utility in the Brewster window in gas lasers, optical broadband angular selectivity, and Brewster angle microscopy.

Methods

Sample fabrication

A polished silicon substrate was cleaned using sequential washes with acetone, alcohol and deionized water, followed by drying with nitrogen gas. Subsequently, a 120 nm thick Ag (99.95%) film was deposited onto the substrate using an ion beam deposition system (SEINAN INDUSTRIES CO., LTDOSAKAJAPAN, SIBD4-5). The Ag-coated substrate was then transferred into the chamber of a Leybold advanced optical deposition system (ARES1100) for the subsequent deposition of Ge films. The purity of the Ge materials used was 99.99%, with the vacuum maintained at 8×10^{-5} Pa, and the deposition temperature set to 200 °C. The evaporation rates of the Ge films were meticulously controlled using a digital proportional-integral-derivative (PID) control system, ensuring precise thickness control facilitated by the optical monitor OMS5000. Finally, the morphologies of the fabricated samples were characterized using SEM (FEI Sirion 200).

Spectrum characterizations

Angle-resolved reflectance spectra of the sample were acquired using a grating spectrometer (Agilent Technologies, Cary 7000) equipped with a reflection module, which facilitated measurements across angles ranging from 6° to 85°.

Ellipsometry characterizations

The refractive indices and thickneses of the Ge, PVA and the refractive indices of Ag coatings (Figs. S3 and S4) were measured using a Variable-angle duarotating-compensator Mueller matrix ellipsometer (ME-L ellipsometer, Wuhan Eoptics Technology Co., Wuhan, China). Additionally, the ellipsometry parameters (Ψ and Δ) as a function of the excitation wavelength were acquired using the same instrument. Measurements were conducted over a broad wavelength range from 380 to 1600 nm with increments of 0.8 nm, and at multiple angles of incidence ranging from 45° to 85° with a step size of 0.1°.

Humidity sensing Tests

PVA procured from Alfa Aesar, with a wide range of molecular weight (MW) distribution ranging from 10000 to 26000 g/mol and an alcoholysis degree of 87% to 89%, was dissolved in deionized water at 90 °C and subsequently cooled to from the resist solution. PVA within this range of MW was selected based on its film quality and solubility. The resist was spin-coated onto Ge films to achieve a film thickness ranging from 40 nm to 50 nm.

A schematic of the gas sensing system is shown in Fig. S7. Various humidity levels (40%, 45%, 50%, 55%, 60%, 65%, 70%, 75%, 80%) inside the sample chamber were adjusted using humidifiers and dehumidifiers. In the experiment, every time when the humidity increases by 5%, wait for about 10 minutes for the PVA to absorb the water completely before starting the test. The temperature in the experiment was kept constant at 24 °C.

References

1. Ma GT, Shen WF, Sanchez DS et al. Excitons enabled topological phase singularity in a single atomic layer. *ACS Nano* **17**, 17751–17760 (2023).
2. Sreekanth KV, Elkabbash M, Medwal R et al. Generalized brewster angle effect in thin-film optical absorbers and its application for graphene hydrogen sensing. *ACS Photonics* **6**, 1610–1617 (2019).
3. Samdani S, Kala A, Kaurav R et al. Reusable biosensor based on differential phase detection at the point of darkness. *Adv Photonics Res* **2**, 2000147 (2021).
4. Sreekanth KV, Han S, Singh R. $Ge_2Sb_2Te_5$-based tunable perfect absorber cavity with phase singularity at visible frequencies. *Adv Mater* **30**, 1706696 (2018).
5. Rao AR, Sreekanth KV, Sreejith S et al. Ultrasensitive detection of heavy metal ions with scalable singular phase thin film optical coatings. *Adv Opt Mater* **10**, 2102623 (2022).
6. Sreekanth KV, Mahalakshmi P, Han S et al. Brewster mode-enhanced sensing with hyperbolic metamaterial. *Adv Opt Mater* **7**, 1900608 (2019).
7. Sreekanth KV, Sreejith S, Han S et al. Biosensing with the singular phase of an ultrathin metal-dielectric nanophotonic cavity. *Nat Commun* **9**, 369 (2018).
8. Berkhout A, Koenderink AF. Perfect absorption and phase singularities in plasmon antenna array etalons. *ACS Photonics* **6**, 2917–2925 (2019).
9. Tan TCW, Plum E, Singh R. Lattice-enhanced fano resonances from bound states in the continuum metasurfaces. *Adv Opt Mater* **8**, 1901572 (2020).
10. Lim WX, Manjappa M, Pitchappa P et al. Shaping high-*Q* planar fano resonant metamaterials toward futuristic technologies. *Adv Opt Mater* **6**, 1800502 (2018).
11. Wang WH, Srivastava YK, Tan TCW et al. Brillouin zone folding driven bound states in the continuum. *Nat Commun* **14**, 2811 (2023).
12. Cong LQ, Singh R. Spatiotemporal dielectric metasurfaces for unidirectional propagation and reconfigurable steering of terahertz beams. *Adv Mater* **32**, 2001418 (2020).
13. Gupta M, Singh R. Terahertz sensing with optimized $Q/V_{\rm eff}$ metasurface cavities. *Adv Opt Mater* **8**, 1902025 (2020).
14. Tian Z, Singh R, Han JG et al. Terahertz superconducting plasmonic hole array. *Opt Lett* **35**, 3586–3588 (2010).
15. Liu MQ, Chen WJ, Hu GW et al. Spectral phase singularity and topological behavior in perfect absorption. *Phys Rev B* **107**, L241403 (2023).
16. Grigorenko AN, Nikitin PI, Kabashin AV. Phase jumps and interferometric surface plasmon resonance imaging. *Appl Phys Lett* **75**, 3917–3919 (1999).
17. Hu JY, Wang Y, Niu JB et al. Observation of dual-polarization topological photonic states at optical frequencies. *Laser Photonics Rev* **17**, 2300515 (2023).
18. Tselikov GI, Danilov A, Shipunova VO et al. Topological darkness: how to design a metamaterial for optical biosensing with ultrahigh sensitivity. *ACS Nano* **17**, 19338–19348 (2023).
19. Song HM, Zhang N, Duan J et al. Dispersion topological darkness at multiple wavelengths and polarization states. *Adv Opt Mater* **5**, 1700166 (2017).
20. Malassis L, Massé P, Tréguer-Delapierre M et al. Topological darkness in self-assembled plasmonic metamaterials. *Adv Mater* **26**, 324–330 (2014).
21. Kravets VG, Schedin F, Jalil R et al. Singular phase nano-optics in plasmonic metamaterials for label-free single-molecule detection. *Nat Mater* **12**, 304–309 (2013).
22. Ermolaev G, Voronin K, Baranov DG et al. Topological phase singularities in atomically thin high-refractive-index materials. *Nat Commun* **13**, 2049 (2022).
23. Ni JC, Huang C, Zhou LM et al. Multidimensional phase singularities in nanophotonics. *Science* **374**, 418 (2021).
24. Yue XZ, Wang T, Yan RQ et al. High-sensitivity refractive index sensing with the singular phase in normal incidence of an asymmetric Fabry–Perot cavity modulated by grating. *Opt Laser Technol* **157**, 108697 (2023).
25. Cusworth E, Kravets VG, Grigorenko AN. Topological darkness in optical heterostructures: prediction and confirmation. *ACS Photonics* **10**, 3715–3722 (2023).
26. Toksumakov AN, Ermolaev GA, Tatmyshevskiy MK et al. Anomalous optical response of graphene on hexagonal boron nitride substrates. *Commun Phys* **6**, 13 (2023).
27. Fonollosa J, Carmona M, Santander J et al. Limits to the integration of filters and lenses on thermoelectric IR detectors by flip-chip techniques. *Sens Actuators A Phys* **149**, 65–73 (2009).

28. Dong M, Zheng CT, Miao SZ et al. Development and measurements of a mid-infrared multi-gas sensor system for CO, CO_2 and CH_4 detection. *Sensors* **17**, 2221 (2017).
29. Anker JN, Hall WP, Lyandres O et al. Biosensing with plasmonic nanosensors. *Nat Mater* **7**, 442–453 (2008).
30. Tan XC, Zhang H, Li JY et al. Non-dispersive infrared multi-gas sensing via nanoantenna integrated narrowband detectors. *Nat Commun* **11**, 5245 (2020).
31. Shi X, Ge LX, Liu BY et al. Optical metasurface composed of multiple antennas with anti-Hermitian coupling in a single layer. *Opt Lett* **46**, 2252–2255 (2021).
32. Shi X, Ge LX, Wen XW et al. Broadband light absorption in graphene ribbons by canceling strong coupling at subwavelength scale. *Opt Express* **24**, 26357–26362 (2016).
33. Li XW, Wen ZJ, Zhou DJ et al. Inverse design of refractory midwave infrared narrowband thermal emitters for optical gas sensing. *Cell Rep Phys Sci* **4**, 101687 (2023).
34. Lv QH, Jin C, Zhang BC et al. Ultrawide-angle ultralow-reflection phenomenon for transverse electric mode in anisotropic metasurface. *Adv Opt Mater* **10**, 2102400 (2022).
35. Lavigne G, Caloz C. Generalized brewster effect using bianisotropic metasurfaces. *Opt Express* **29**, 11361–11370 (2021).
36. Zhang Z, Che ZY, Liang XY et al. Realizing generalized brewster effect by generalized kerker effect. *Phys Rev Appl* **16**, 054017 (2021).
37. Tamayama Y, Nakanishi T, Sugiyama K et al. Observation of brewster's effect for transverse-electric electromagnetic waves in metamaterials: experiment and theory. *Phys Rev B* **73**, 193104 (2006).
38. Watanabe R, Iwanaga M, Ishihara T. S-polarization brewster's angle of stratified metal-dielectric metamaterial in optical regime. *Phys Status Solidi Res* **245**, 2696–2701 (2008).
39. Kats MA, Blanchard R, Genevet P et al. Nanometre optical coatings based on strong interference effects in highly absorbing media. *Nat Mater* **12**, 20–24 (2013).
40. Pan H, Wen ZJ, Tang ZH et al. Wide gamut, angle-insensitive structural colors based on deep-subwavelength bilayer media. *Nanophotonics* **9**, 3385–3392 (2020).
41. Tompkins HG, Hilfiker JN. *Spectroscopic Ellipsometry: Practical Application to Thin Film Characterization* (Momentum Press, New York, 2016).
42. Fan SH, Suh W, Joannopoulos JD. Temporal coupled-mode theory for the fano resonance in optical resonators. *J Opt Soc Am A Opt Image Sci Vis* **20**, 569–572 (2003).
43. Suh W, Wang Z, Fan SH. Temporal coupled-mode theory and the presence of non-orthogonal modes in lossless multimode cavities. *IEEE J Quantum Electron* **40**, 1511–1518 (2004).
44. Wang B, Liu WZ, Zhao MX et al. Generating optical vortex beams by momentum-space polarization vortices centred at bound states in the continuum. *Nat Photonics* **14**, 623–628 (2020).
45. Wang ZJ, Dai CJ, Zhang J et al. Real-time tunable nanoprinting-multiplexing with simultaneous meta-holography displays by stepwise nanocavities. *Adv Funct Mater* **32**, 2110022 (2022).
46. Zhang J, Huang C, Chen YX et al. Polyvinyl alcohol: a high-resolution hydrogel resist for humidity-sensitive micro-/nanostructure. *Nanotechnology* **31**, 425303 (2020).

Acknowledgements

This work was supported by the National Key R&D Program of China (2022YFA1404701), Program of Shanghai Academic Research Leader under Grant (22XD1422100), National Natural Science Foundation of China (62075231, 12141303, 12073018), Shanghai Science and Technology Committee (20JC1414603, 23dz2260100), Shanghai Pujiang Program (21PJ1411400), China Postdoctoral Science Foundation (2021M703335), Young Elite Scientists Sponsorship Program by CAST (YESS20220355).

Competing interests

The authors declare no competing financial interests.

Supplementary information

Supplementary information for this paper is available at https://doi.org/10.29026/oea.2024.240091